β-Sn grain-boundary structure and self-diffusivity via molecular dynamics simulations

Michael S. Sellers,[1] Andrew J. Schultz,[1] Cemal Basaran,[2] and David A. Kofke[1]
[1]*Department of Chemical and Biological Engineering, University at Buffalo, The State University of New York, Buffalo, New York 14260, USA*
[2]*Electronics Packaging Laboratory, Department of Civil, Structural and Environmental Engineering, University at Buffalo, The State University of New York, Buffalo, New York 14260, USA*

(Received 19 January 2010; revised manuscript received 1 April 2010; published 26 April 2010)

The self-diffusion properties of several β-Sn symmetric tilt grain boundaries are examined using molecular dynamics simulations. The boundary types examined—(101), (201), (401), (310)-Σ5, and (410)—are chosen from those observed in experiment and from arbitrary Miller planes, giving a variety of tilt angles and interface properties. Planar structure factor and diffusivity profiles for each boundary are computed and a grain-boundary width, δ_{GB}, is measured from these profiles. Larger diffusive widths (δ_{GB}) are exhibited by higher excess potential energy grain boundaries. Diffusivities (D_{GB}) in the directions parallel to the interface plane are computed and activation energies are found with the Arrhenius relation. D_{GB} (as $\delta_{GB}D_{GB}$ normalized by δ_{GB}) is shown to agree well with experiment. We also investigate the anisotropic diffusive behavior of the (401) grain boundary and find that the low energy grain boundary exhibits very low activation energy diffusion, due to the development of diffusive channels.

DOI: 10.1103/PhysRevB.81.134111 PACS number(s): 66.30.−h, 31.15.xv, 61.72.Mm, 06.60.Vz

I. INTRODUCTION

Grain boundaries in metals provide fast-diffusion paths for solute and solvent atoms.[1,2] These boundaries are often present in electronics packaging components, and diffusion processes occurring through them can contribute significantly to loss of the structural integrity of the component.[3] These processes are enhanced by the presence of thermal and electrical gradients. Thermomigration and electromigration, two phenomena known to plague Sn-Ag-Cu solder joints, describe the temperature- and electrical-current-induced atomic flux, respectively. As atoms move though the grain boundaries, vacancies are squeezed in the opposite direction and coalesce at the cathode, causing large void creation leading to cracking and eventual joint failure.

Models of these processes in Al and Sn continue to develop and many are based on quantities that describe atomic level processes. Stress due to a single vacancy, effective valence of solvent atoms, and grain-boundary self-diffusivities all play a role in the vacancy flux equation, which captures the effects of electrical current, concentration, temperature, and stress on the flow of vacancies in a metal.[4] Although able to predict qualitative trends,[5] these models currently lack the microstructural detail necessary for accurate failure rate prediction. As they improve, knowledge of the transport within specific microstructures will help to fully describe the behaviors being modeled. Specifically, diffusivities for different types of grain boundaries, and a description of the boundary behavior with temperature will be critical in modeling microstructure evolution.

Few experimental diffusion studies have been conducted on Sn grain boundaries, but activation energies obtained from experimental work on diffusion in bulk Sn have been determined, and span a range of values.[6–8] Sun and Ohring suggested that some authors who report low activation energies may in fact be unknowingly measuring grain-boundary diffusion.[8] Results from a significant number of bulk Sn studies are compiled in their work and reveal that grain-boundary diffusion activation energies fall in a distinct range. In a follow-up study on polycrystalline Sn, Singh and Ohring measured grain-boundary diffusivity at low and high temperatures.[9] Their high-temperature results match well with a cited second study on grain-boundary diffusion and the values from Singh and Ohring's work are used in many studies of solder joint damage. One example is a finite-element simulation incorporating β-Sn, Ag, and Cu diffusivities providing overall "solder joint diffusive activation energies" backed out of time-to-failure measurements.[10]

As a complement to experimental work, molecular simulation serves to reinforce these quantitative predictions and provide more insight into the atomistic processes that govern them. In the present study, we employ molecular dynamics (MD) simulation to determine grain-boundary diffusivity of specific β-Sn grain boundaries. Although a significant amount of simulation work has been completed on grain boundaries in various materials and by a variety of methods,[11–16] we believe this is the first to study β-Sn grain boundaries. We compare our results of diffusivities calculated in grain-boundary structures to Singh and Ohring's average β-Sn grain-boundary diffusivity and activation energy. Recent work by Telang and Bieler shows the consumption and growth of particular grains of Sn when a polycrystalline sample is subjected to stress and high-temperature anneal.[17,18] The specific grain-boundary structures that persist in their work form the basis for the range of structures we study here. Notably, they see an increase in the number of (101) and (301) symmetric tilt grain boundaries present in their samples after separate stress and heat trials.[18] We construct these two types of boundaries in simulation, and include other structures that are of a similar grain-boundary character. The range of grain boundaries studied can describe an average diffusivity one might expect in a polycrystalline sample, yet also exhibit individual behavior worthy of investigation.

The paper follows with Sec. II in diffusivity measurement and grain-boundary characterization. Next, in Sec. III we outline our specific grain-boundary structure choices and their minimization. We then present and discuss our results in Sec. IV and follow up with concluding remarks in Sec. V.

II. METHODOLOGY

β-Sn phase grain boundaries in this work are created with custom Java code and modeled using the modified embedded-atom method (MEAM) (Ref. 19) with MD simulations conducted in the LAMMPS molecular simulation package.[20,21] Specific choice of grain boundary and details about system minimization are explained in Sec. III, and we continue here with an explanation of our methods of diffusivity calculation and interface characterization.

A. Diffusivity calculation

Typically, self-diffusion in an MD simulation is measured via the Einstein or Green-Kubo relations, which involve tracking atomic displacements or velocities.[22] We choose to follow the work of Keblinski *et al.*,[16] wherein diffusion is measured with an adjusted form of the Einstein relation. The setup of our grain boundaries requires this. In a particular MD run, atoms close to the grain boundary will exhibit a variety of displacement lengths. However, as one moves away in a direction perpendicular to the interface, displacement begins to decrease to the order of atomic vibrations. Averaging the squared displacement over all atoms, as is normally done, would reduce the true value of solvent self-diffusivity in the grain boundary. In addition, the transition between fast and nonexistent diffusivity regions for each grain boundary is not known *a priori*, removing the simple method of specifying a diffusing volume. Instead, we compute the total squared displacement in our system and normalize this quantity by atomic volume per grain-boundary area, shown in Eq. (1).

$$\delta_{GB}D_{GB} = \frac{\Omega N_A}{A}\frac{1}{4}\frac{dMSD}{dt}. \tag{1}$$

Here, Ω is the volume per Sn atom in our system, N_A is the number of atoms used to compute the mean squared displacement, A is the interfacial area, and the factor of 1/4 is determined by the dimensionality of the mean squared displacement (MSD). After this scaling, the quantity computed is likened to the interface width δ_{GB} perpendicular to the plane of A, multiplied by the true grain-boundary diffusivity, D_{GB}. Now, δ_{GB} may be represented as shown in Eq. (2), where N_D is now the number of diffusing atoms.

$$\delta_{GB} = \frac{N_D\Omega}{A} \tag{2}$$

During a particular simulation run, the total squared displacement ($N_A \times$MSD) is calculated and with Eq. (1), yields the quantity $\delta_{GB}D_{GB}$. Furthermore, and as we present later in this work, our grain boundaries show a variety of interface widths, so we must determine δ_{GB} by means other than Eq. (2) to finally resolve a value of D_{GB} for different grain boundaries.

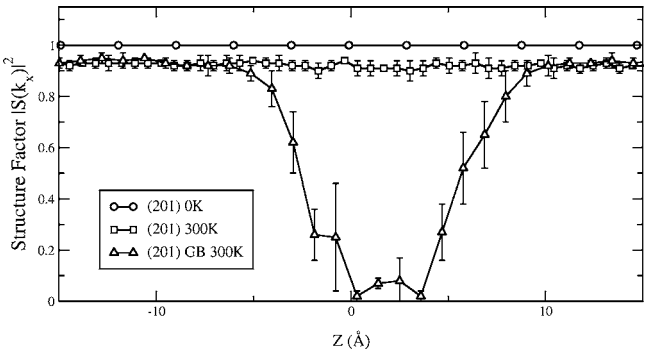

FIG. 1. The variation in $|S(k)|^2$, for a bulk solid at 0 and 300 K, and a grain boundary at 300 K. Note the abscissa is the direction perpendicular to the interface. Error bars represent the standard deviation of $|S(k)|^2$ in five snapshots of an MD run.

B. Interface width calculation

D_{GB} is evaluated post-MD run by examining the diffusive and structural profiles of each grain boundary simulated, computing a δ_{GB} value from these profiles via a *full-width-at-half-maximum* analysis, and normalizing the MD sampled $\delta_{GB}D_{GB}$. For a particular grain boundary, we compute planar quantities of the diffusivity and squared structure factor in directions perpendicular to the grain-boundary interface and establish a fixed value of δ_{GB} at a given temperature. Planar diffusivity is calculated using a typical Einstein relation for atoms in a plane. We restrict the volume of space in which MSD is sampled to slices in successive z planes, where D_{xy} is the slope of this quantity versus time. Shown in Eq. (3) is the relation for the squared structure factor, $|S(k)|^2$.

$$|S(\vec{k})|^2 = \frac{1}{N^2}\left[\left(\sum_{i=1}^{N}\cos(\vec{k}\cdot\vec{r})\right)^2 + \left(\sum_{i=1}^{N}\sin(\vec{k}\cdot\vec{r})\right)^2\right]. \tag{3}$$

In this case, k is a wave vector that describes the periodicity of the perfect lattice in a particular direction, r is the position of the atom contained in the plane, and N is the number of atoms in the plane. Depending on the current structure's deviation from the perfect lattice, the quantity $|S(k)|^2$ can range from 1 (identical structure to the wave vector) to 0 (no structure with respect to the wave vector). This provides a good measure of the structural transition that develops at or around the grain-boundary interface (Fig. 1).

Many works employ a measure of the interface structure to investigate thermodynamic phase and interface width.[13–16] The use of a potential energy profile per plane has also been used to determine δ_{GB}.[13,16] For our work, both the diffusive and structural widths provide information about how the grain-boundary interfaces evolve with Miller plane type and simulation temperature, but we use only the diffusive width in the calculation of D_{GB} from the quantity $\delta_{GB}D_{GB}$ measured in simulation. Values of δ_{GB} calculated from a planar diffusion measurement are more closely related to the total squared displacement we are measuring in simulation. There-

FIG. 2. (Color online) The three systems considered in excess potential energy calculations. Orange lines are Miller planes; green dashed lines are fixed free surfaces.

fore, we believe the most accurate grain-boundary diffusivity, D_{GB}, is computed using the diffusive width measurements.

C. Excess potential energy calculation

A single value describing the grain boundary's energetic deviation from a bulk system at a given temperature can be used to differentiate it with respect to other grain-boundary structures. Computation of this quantity is fairly straightforward and can be done at various temperatures during simulation. Because of our system setup, as shown in Fig. 2, we use an intermediary structure to remove the effect of the two free surfaces present in our simulations. From here we can obtain a measure of the excess potential energy of the grain-boundary interface only.

Shown in Eq. (4) and used in several works[23,24] is the excess grain-boundary potential energy γ_{GB}, where E_{GB} is the potential energy of the grain-boundary structure, E_{SLAB} is the energy of the tilted slab structure, and the quantity $N_{X,ATOMS} \times E_{BULK,ATOM}$ is the energy of a periodic bulk structure with the same number of atoms as the slab or grain boundary. Finally, γ_{GB} is scaled by the interface area A. We note that Eq. (4) can be simplified but is left in expanded form for clarity. Starting with the potential energy of the grain-boundary system, we remove the energy increase due to the upper and lower free surfaces (second term of the numerator) and then compare the remaining energy to that of a fully periodic structure of the same number of atoms (third term).

$$\gamma_{GB} = \frac{E_{GB} - (E_{SLAB} - N_{SLAB,ATOMS} \cdot E_{BULK,ATOM}) - (N_{GB,ATOMS} \cdot E_{BULK,ATOM})}{A}. \tag{4}$$

III. SIMULATION DETAILS

A. Interatomic potential

To characterize the atomic interactions of Sn, we use the MEAM, developed by Baskes. The development of the potential is outlined below and details are given in Refs. 25 and 26,

$$E = \sum_i \left[F_i\left(\frac{\bar{\rho}_i}{Z_i}\right) + \frac{1}{2}\sum_i \phi(r_{ij}) \right]. \tag{5}$$

The energy that an atom E_i contributes to the total energy of a system E through interactions with its neighbors is given above. F is the embedding function, or the energy required to embed an atom of type i in to the background electron density ρ_i. This factor is normalized by Z_i, the number of nearest neighbors in the reference structure. The second term, $\phi(r_{ij})$, is the pair interaction between atom i, and its neighbors, j. Sn parameters are listed in Table I.[27]

These parameters are determined by fitting experimental values of Sn's bulk modulus, average atomic volume, cohesive energy, and equilibrium nearest-neighbor distance of a reference structure of FCC lattice packing. As reported in Ref. 27, the potential for Sn has successfully reproduced experimental values of the heat capacity for Sn's α and β phases, as well as the phase-transition temperature between liquid and β-Sn, and β and α-Sn. Details on MEAM's implementation in LAMMPS are available elsewhere. [19]

The β-Sn phase, one of two allotropes of Sn, is metallic and stable at temperatures above 286 K to Sn's melting point of 505 K. It adopts a body-centered-tetragonal structure with lattice constants of $a=5.831$ Å and $c=3.182$ Å (Fig. 3). Using the MEAM potential, the equilibrium lattice constants are $a=5.92$ Å and $c=3.23$ Å, preserving the 0.546 c/a ratio observed experimentally, while the melting temperature is lowered in comparison to experiment, to 453 K.

B. Structure development and minimization

We construct various types of symmetric tilt grain boundaries, which can be thought of as twist grain boundaries with 180° rotation.[16] The specific types of grain boundaries simulated are limited to structures that are of medium to high energy, and whose interface atoms exhibit enough motion at

TABLE I. Parameters for the MEAM potential.

	$\mathbf{E_C}$ (eV)	$\mathbf{r_0}$ (A)	$\boldsymbol{\alpha}$	A	$\boldsymbol{\beta^{(0)}}$	$\boldsymbol{\beta^{(1)}}$	$\boldsymbol{\beta^{(2)}}$	$\boldsymbol{\beta^{(3)}}$	$\mathbf{t^{(1)}}$	$\mathbf{t^{(2)}}$	$\mathbf{t^{(3)}}$	$\boldsymbol{\rho_0}$
Sn	3.08	3.44	6.20	1.0	6.2	6.0	6.0	6.0	4.5	6.5	−0.183	1.0

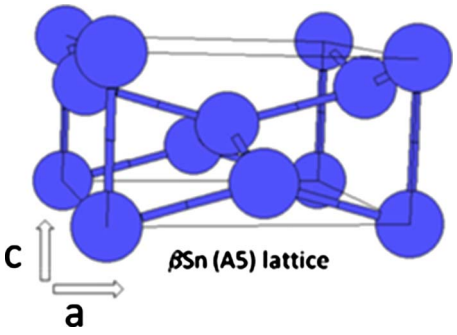

FIG. 3. (Color online) β-Sn crystal structure (Ref. 28).

our simulation temperatures to compute an accurate diffusivity. Symmetric tilt grain boundaries that fall under these categories with shared interfacial Miller planes (hkl) of (h01) and (h10) are: (101), (201), (401), tilted around [010], and (310)-Σ5, and (410), tilted around [001], shown in Fig. 4. We can also say that the 0 Miller index value of the plane denotes the axis that the two grains are independently rotated around to expose their common Miller plane.

In general, there are two types of simulation setups. The first involves a fully periodic simulation box, with repeating structural units in the x, y, and z directions. This particular technique is used in many works, such as in Ref. 13. Here one must create two grain boundaries such that the top and bottom of grain 1 creates interfaces with grain 2. This enables periodicity in a direction perpendicular to the grain boundary. The second type removes the periodic nature of the simulation box in the direction perpendicular to the grain boundary, and fixes atoms at the top of grain 1 and at the bottom of grain 2, mimicking a bulk structure and creating a periodic "sandwich."[16] In this case it is important to equilibrate the system correctly in order to obtain a zero average pressure. For this work we use the latter method, as this system often contains fewer atoms than the fully periodic, dual interface structure.

The process of minimization of the grain boundary is done in two steps. First, near 0 K the two grains move independently in x, y, and z directions via molecular dynamics, their respective atoms all having the same average force each time step. This step is shown in Fig. 5: *minimization*. An investigation in NiAl alloy grain boundaries by Mishin and

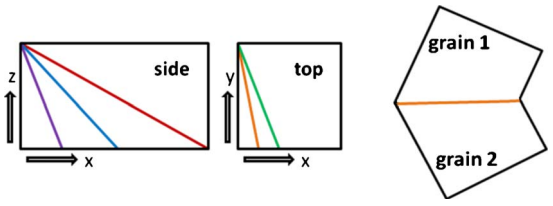

FIG. 4. (Color online) Shown left are various Miller planes in β-Sn's lattice. Right is the rotation of two grains to share a common Miller plane. Red, blue, and purple are (101), (201), and (401) Miller planes, respectively. Green and orange are (310) and (410), respectively. Note that the *side* view x direction is stretched for figure height conformity. X direction corresponds to the lattice a direction, [100]; Z direction corresponds to the lattice c direction, [001].

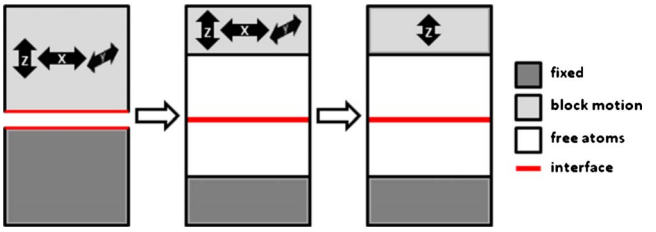

FIG. 5. (Color online) Minimization (near 0 K-MD), equilibration, and production structures. Actual simulation cells are three-dimensional and periodic in x and y directions.

Farkas[24] employed the γ-surface technique to map out the energy surface created by the two static moving grains. We do not employ this technique; however our 0 K minimized structures do find lower energy configurations relative to their initial structure. Once a minimum-energy structure has been found, the system is then equilibrated at the desired production run temperature (Fig. 5: *equilibration*). Here, atoms in the bottom grain within twice the potential cutoff distance of the bottom edge of the structure are fixed and atoms in the top grain within twice the potential cutoff distance of the top edge of the structure are given an average force in the x, y, and z directions. This creates a floating boundary at the top of the box and allows the system to reach an average zero pressure over 100 ps. Following these steps, the floating boundary is now fixed and the grain boundaries are simulated between 2 and 4 ns (Fig. 5: *production*).

IV. RESULTS AND DISCUSSION

With MD we simulated five medium to high energy β-Sn symmetric tilt grain boundaries. Specifically, boundaries with grains that share the (101), (201), (401), (310), and (410) Miller planes at their interface. For each grain boundary, we computed the excess potential energy at 300 K from an average value sampled over the course of our molecular dynamics production runs. We also computed $\delta_{GB}D_{GB}$ during the simulations and estimated the value of δ_{GB}, the grain-boundary diffusive width, at temperatures from 300 K to 450 K. From here we calculated D_{GB} for all boundaries in the temperature range and examined more closely directional diffusion in the interface of the (401) grain boundary.

A. Grain-boundary excess potential energies

An often adequate measure of the order at the grain-boundary interface and a characteristic of its transport behavior is the excess potential energy of a grain boundary. Outlined in a previous section, this quantity is the extra energy resulting from the low coordination of interface atoms. Shown in Table II are computed excess energies of the five grain boundaries studied in this work. It is clear from these calculations that, depending on the Miller plane chosen, there exists a different degree of lattice mismatch, corresponding to an excess energy value. For the (101), (201), and (401) grain boundaries, the excess grain-boundary energy decreases with increasing h index. However, for the (310) and

TABLE II. Excess interfacial potential energies (mJ/m^2) at 300 K.

GB (K)	(101)	(201)	(401)	(310)	(410)
300	1089.68	364.08	198.98	338.76	343.44

(410) planes, the energy slightly increases with increasing h index.

B. Width-scaled diffusivity ($\delta_{GB}D_{GB}$) from molecular dynamics

Results from squared displacement samples are shown in Fig. 6. Here we plot in Arrhenius form the scaled diffusivity, $\delta_{GB}D_{GB}$, versus temperature. In addition to data from our grain-boundary simulations, experimental scaled diffusivity values from Singh and Ohring[9] are shown as dark lines. These lines represent the two different experimental relationships used to analyze the concentration profiles of Sn radiotracer in polycrystalline thin films. Arrhenius parameters for the experimental data plotted in Fig. 6 are shown in Table III.

We can see from Fig. 6 that the $\delta_{GB}D_{GB}$ values for the simulated grain boundaries, with the exception of the (401) grain boundary, behave in a trend relative to their excess potential energies. For example, the (101) grain boundary exhibits the highest excess energy and the highest width scaled diffusivity. When compared to experiment at low temperature, the simulated boundaries show good agreement with experimental work. Magnitudes of the width scaled diffusivity at low temperature are all within the error reported in Ref. 9 and reproduced in Table III. An argument could be made about the large discrepancy in slope (diffusive activation energy) at low T; however, when considering statistical uncertainty the slopes appear similar for many of the grain boundaries. This point will be discussed later in our analysis of D_{GB}.

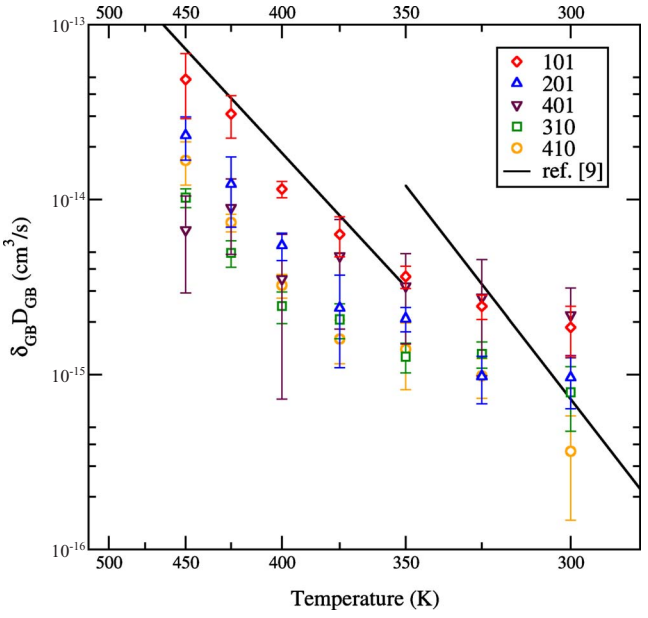

FIG. 6. (Color online) Arrhenius plot of scaled diffusivity vs temperature. Points are results for various symmetric tilt grain boundaries simulated in this work. Dark lines are experimental data from Singh and Ohring (Ref. 9). Error bars represent standard deviation of three independent simulations and computations of $\delta_{GB}D_{GB}$.

Continuing the comparison to higher temperatures, all our boundaries fall, at most, within one order of magnitude of experimental values and show a similar trend in slope. Further comparison of diffusivities is done by calculating D_{GB} using values of δ_{GB} for each grain boundary at a range of temperatures.

C. Grain-boundary width calculation

To investigate possible changes in interface width with particular grain boundaries and/or temperature, we calculated planar profiles of diffusivity and structure in planes parallel to the grain-boundary interface. For every grain boundary, at temperatures from 300 to 450 K, diffusive and structural widths were calculated using methods outlined in the previous section. Shown below are two figures representing results from calculations of δ_{GB}. The first, Fig. 7, presents planar diffusivity profiles of the five grain boundaries studied in this work. We have selected temperatures of 300 and 450 K to display.

As shown in Fig. 7 for a temperature of 300 K, we see an increase in planar diffusivity and an increase in diffusive width with increasing grain-boundary energy. Here, the (401) boundary exhibits a relatively high diffusivity with a narrow width. For 450 K, the (401) grain boundary again displays similar behavior, while the other boundaries now have a diffusivity within the same order of magnitude. Also, at higher temperature, the boundaries are shown to maintain their diffusive widths.

In addition to measuring the width via planar diffusion, we investigated the structural behavior of each grain boundary. Figure 8 shows plots of the squared planar structure factor for each grain boundary. Each illustrates a change in the boundary's structure with temperature. The type of

TABLE III. Arrhenius properties calculated from experiment in Ref. 9.

	300–350 K	350–450 K
D_{GB} (10^{-8} cm^2/s)	1.45 (300 K)	6.34 (350 K)
δ_{GB} (10^{-8} cm)	5.0 (assumed)	
$\mathbf{E_A}$ (eV)	$0.50^{+/-0.04}$	0.4245
$\mathbf{D_0}$ (10^{-2} cm^2/s)	$490^{+1560/-370}$	8.3

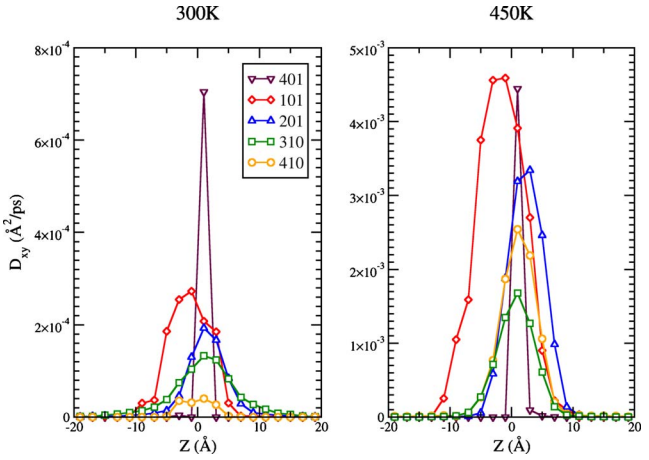

FIG. 7. (Color online) Planar diffusivity for various grain boundaries at 300 (left) and 450 K (right). Note the different scales for each temperature, but similar scales for z. Lines are guides for the eyes.

change varies between grain boundaries, but we note for the (101) and (201) grain boundaries, as we approach 450 K the disordered structure at the interface grows in a widthwise fashion. For (401) and (410) the width is maintained, yet the amount of disorder changes with temperature. In Fig. 9, we include simulation snapshots for the (101) grain boundary at temperatures of 300 and 450 K. For views oriented parallel to the grain-boundary tilt axis, we see a slight decrease in ordering (increase in width) at the lattice-interface plane when comparing 300–450 K.

Diffusive and structural widths for each grain boundary are compiled and plotted versus temperature in Fig. 10. We also include the value used in the experimental work, δ_{GB} =5.0 Å. From Fig. 10 we can see that each grain boundary exhibits different widths. While not as distinct as the magnitudes of diffusivity, the high energy grain boundary shows the largest width, medium energies show slightly smaller widths, and the low energy (401) shows the smallest width. Contrasting the two types of analysis, diffusive and structural, we see that the diffusive width remains relatively constant while the structural is more dynamic and increases with temperature for a few of the boundaries.

For the two boundaries ((101) and (201)) that show slight increases in their structural width with temperature, we also observe a large degree of disorder at the interface. Compared to the other plots in Fig. 8, these two boundaries exhibit almost no structure when compared to β-Sn's bulk lattice. The extreme of this scenario is evidence of a large increase in grain-boundary width and a transition to liquidlike disorder with an increase in temperature at points below the material's bulk melting point. This is referred to in literature as a "premelting" transition. Previous work by Keblinski *et al.*[16] on molecular dynamics simulations of face-centered cubic Pd grain boundaries asserts the existence of grain boundary premelting at temperatures below the bulk melting temperature. Their high energy boundaries undergo a transition to a confined liquid structure at a critical temperature dependent on boundary energy. Evidence of this liquid structure transition is given by a change in diffusion activation energy and a

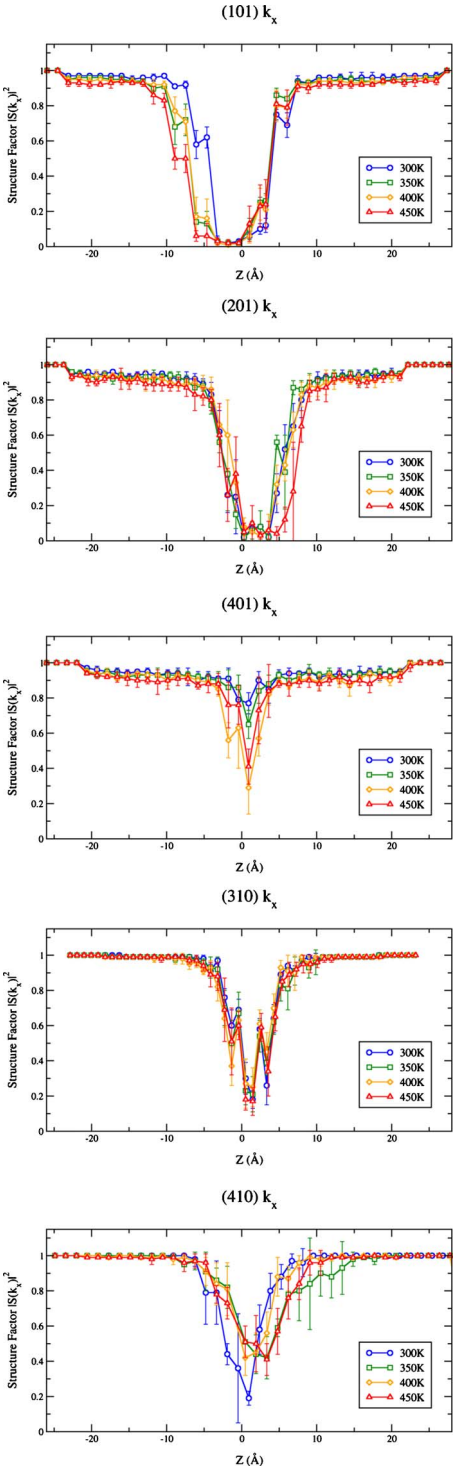

FIG. 8. (Color online) Square planar structure factor vs z-axis plane for the five grain boundaries studied. Colors are different temperatures. Blue 300 K, green-350 K, orange-400 K, red 450 K. Error bars represent the standard deviation of $|S(k)|^2$ in five snapshots from an MD run.

diffusivity that increases to a value close to the liquid value at the melting temperature. An earlier study by Ciccotti *et al.* of Lennard-Jones (310)-Σ5 grain boundaries found only partial structural disorder in this boundary as the melting point is approached. In their analysis, they compute a grain-

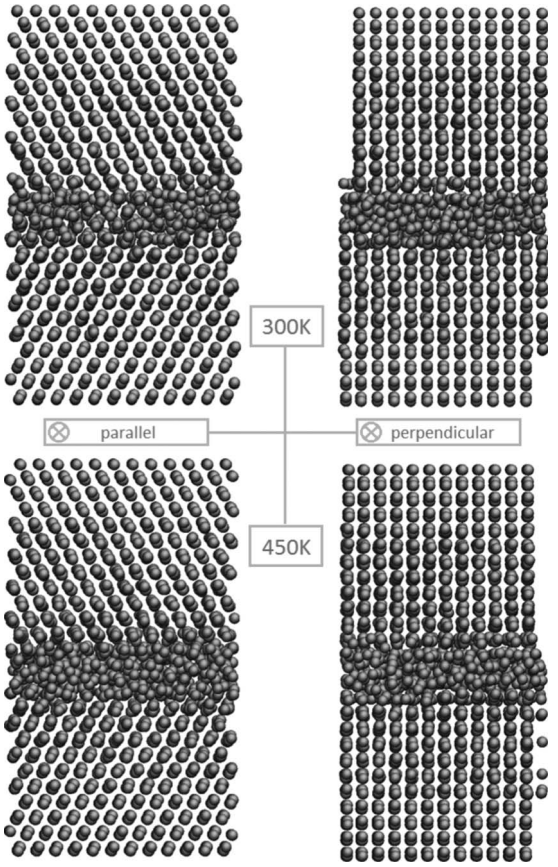

FIG. 9. TOP and BOTTOM are snapshots of the (101) GB at 300 and 450 K, respectively. Left is looking parallel to the grain tilt axis and at right looking perpendicular.

boundary diffusivity for their system near the melting point that is below the supercooled liquid value at the same temperature.[15] In another study by Suzuki and Mishin, where Cu (210)-Σ5 and (310)-Σ5 grain boundaries were simulated up to the melting point, they did not see any evidence of premelting in their systems. They do note however, that all

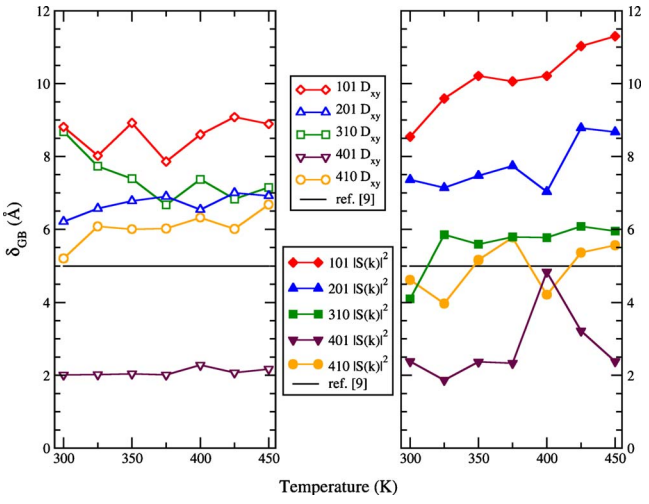

FIG. 10. (Color online) Diffusive (open points, left) and structural widths (filled points, right) versus temperature for the five grain boundaries studied. Lines are guides for the eyes.

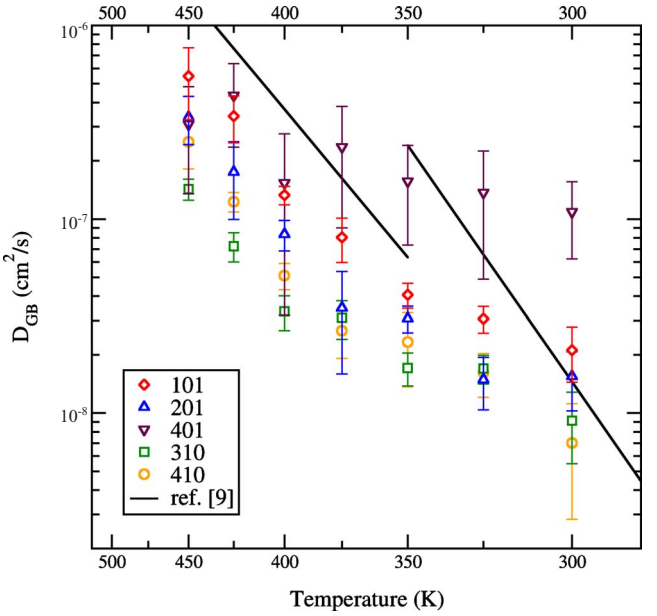

FIG. 11. (Color online) An Arrhenius plot of grain-boundary diffusivity vs temperature. Shown as colored points are various symmetric tilt grain boundaries simulated in this work. Dark lines are experimental data from Singh and Ohring. Error bars represent standard deviation of three or more independent simulations.

the grain boundaries collapse on a common self-diffusivity close to the melting temperature.[14] Similar to reports in literature, the various studies of structure and dynamics in our grain boundaries do not explicitly show that premelting is occurring for β-Sn. We do see disordered interfaces develop for the (101) and (201) grain boundaries and they remain stable throughout the temperature range studied in this work. While this may suggest the notion of premelting in our boundaries, the foundation of its existence is dependent on a change in slope of the grain-boundary diffusivity. D_{GB} at high temperature must also present a value close to liquid self-diffusivity as the melting point is approached. Upon further analysis, detailed in the next section, we see no change in the slope of D_{GB} as temperature is increased and magnitudes that do not approach the liquid diffusivity as the melting point is approached. We can therefore say that although some of our simulated interfaces show disorder, none exhibit the premelting phenomenon.

D. Resolving the grain-boundary diffusivity (D_{GB})

Using values of the diffusive width (δ_{GB}) for each temperature and grain-boundary type, we now resolve D_{GB} for each grain boundary, and remove the effect of δ_{GB}'s variation with grain-boundary type on $\delta_{GB}D_{GB}$ previously shown in Fig. 6. Here, the specific grain-boundary self-diffusivity, D_{GB}, for each type studied in this work is shown in Fig. 11. The standalone data in Fig. 11 is the (401) grain boundary. It now shows its true diffusivity in comparison to the other simulated grain boundaries. Although the width is small, the low energy (401) boundary exhibits fast, low activation energy, diffusion. This behavior is given further study in the next section. Singh and Ohring report values of D_{GB} using

TABLE IV. Arrhenius properties of simulated grain boundaries from weighted least-squares fit, 325–450 K.

GB	(101)	(201)	(401)	(310)	(410)
$D_{GB\text{-}300\ K}$ (10^{-8} cm^2/s)	2.11	1.55	10.9	0.914	0.700
$\mathbf{E_A}$ (eV)	0.263(4)	0.295(5)	0.10(1)	0.22(5)	0.274(7)
$\mathbf{D_0}$ (10^{-4} cm^2/s)	2.9(4)	6(1)	0.08(5)	2.2(8)	40(2)

δ_{GB}=5.0 Å to adjust their experimentally measured values of $\delta_{GB}D_{GB}$. This is also plotted in Fig. 11. Compared to Fig. 6 and relative to Singh and Ohring's reported values, we see similar trends from the (201), (310), and (410) grain boundaries. For the (101) grain boundary, the magnitude of D_{GB} has shifted slightly lower relative to the experimental results. Our low-temperature values, 300 K to 350 K, still fall within the error in Singh and Ohring's results, outlined in Table III (though no error is listed for high temperature), and all our values are still within one order of magnitude of experiment. It is important to mention finally that using any value larger than δ_{GB}=5.0 Å with the experimental results will decrease the gap between it and simulation. The authors of Ref. 9 do not mention the significance of this value for β-Sn, although in other works, when used in analytical expressions, it is shown to match experimental results in higher melting point materials, such as Ag.[29]

The slopes of simulation data from 350 to 450 K show good agreement with experiment. At low temperatures of 300 and 325 K however, average values from multiple simulations create a low-slope region. This behavior is similar to that in Fig. 6 and is maintained even after removing the influence of width. While the amount of error shows that statistically, these points may have a slope that is similar to higher temperature data, we've restricted the analysis of D_{GB} to values simulated at temperatures of 325–450 K. We believe the large error at 300 K arises from poor sampling because of the time scale constraints of molecular dynamics. A weighted least-squares fit is applied to Fig. 11 diffusion data in this temperature range to calculate Arrhenius parameters for each grain boundary. These are shown in Table IV.

E. Analysis of in-plane directional diffusivity

In Fig. 11 and Table IV, we see a contrast in slope of the (401) grain boundary when compared to other low D_{GB} grain boundaries [e.g., (310), (410)]. While of low excess potential energy and therefore high atomic coordination at the interface, the activation energy of diffusion in this grain boundary is low. This duality is indicative of possible channel structures forming at the interface in a single direction.[1] Accordingly, we investigated the development of any anisotropy in diffusivity in the plane of the grain-boundary interface. Shown in Fig. 12 are plots of (h10) and (h01) grain boundaries and their respective $\delta_{GB}D_{GB}$ component values. For both plots, diffusion in the direction parallel to the grain tilt is shown as open points and diffusion perpendicular to the grain tilt is shown as filled points. For the (310) and (410) grain boundaries, shown in the left plot, self-diffusion in either direction is essentially equivalent. For the (101), (201), and (401) however, as the h index of the grain boundary is increased, a degree of anisotropy in the diffusion coefficient develops.

If we focus on the (401) grain boundary, we can see a high degree of directional diffusivity. This is also evidenced in simulation snapshots, shown below in Fig. 13. By inspection, the structure of the (401) grain boundary is much more evident in a view down the grain tilt axis ([010]), as shown in the parallel view direction of Fig. 13. Conversely, the perpendicular view direction of this figure shows a thin interface with disordered atoms.

We can explain the behavior of the (401) grain boundary in Figs. 11–13 by first referencing the β-Sn crystal structure. It has been shown in experiment that diffusion in the c direction of the bulk crystal proceeds much more slowly than diffusion in the a direction.[6,7] When we identify the crystal orientation in these grain boundaries, we notice that for increasing Miller index in the h01 boundaries, the interface adopts more of the c direction of the bulk lattice. This behavior is shown in Fig. 4, where in moving from the (101) to (201) to (401), red to blue to purple in the figure, the interface shared by the two grains increasingly aligns with the c direction of the lattice. The β-Sn bulk lattice anisotropy does not explain the loss of structure, however. The simulation snapshots in Fig. 13 show a disordered structure parallel to

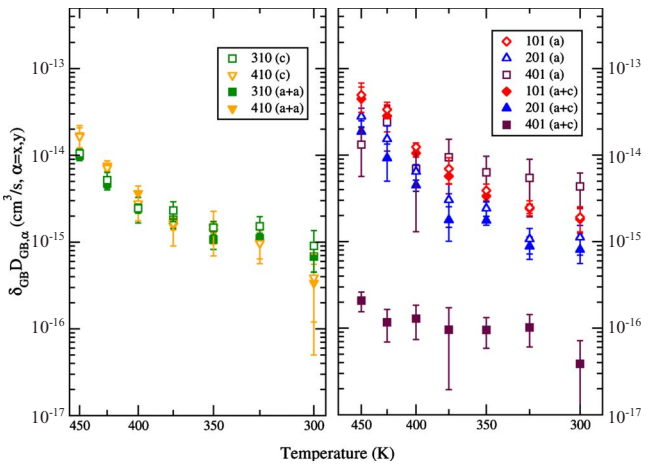

FIG. 12. (Color online) Arrhenius plots of scaled directional diffusivity vs. temperature. Left are (310) and (410) grain boundaries, Right are (101), (201), and (401) grain boundaries. Filled points are diffusion in a direction perpendicular to the grain tilt axis; open points are diffusion in a direction parallel to the grain tilt axis. Letters in parentheses in the plot legends are crystal lattice directions of diffusion. Error bars represent standard deviation of three or more independent simulations.

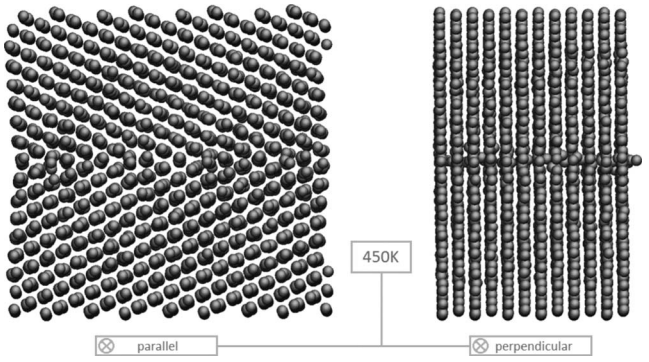

FIG. 13. Simulation snapshot of (401) grain boundary at 450 K. Left is looking down the grain tilt axis and at right the grain tilt axis is oriented left/right.

the grain-boundary interface and parallel grain tilt direction (shown in the perpendicular view). This can be explained by the existence of channels in the interface that aid in fast solvent and solute diffusion. We can say at this point that the (401) grain boundary's anisotropic diffusivity is a function of both the tetragonal crystal structure, and the formation of structural channels.

V. CONCLUSIONS

This work investigated diffusion in five grain boundaries, the (101), (201), (401), (310), and (410) symmetric tilts. Our structures are based on those shown to exist in experiment and those that exhibit sufficient motion for squared displacement calculations during molecular dynamics simulations at temperatures of 300 to 450 K. We find that $\delta_{GB}D_{GB}$ is not the most effective way to describe the transport behavior of these grain boundaries. One must also investigate the boundary's interface width.

By determining the structural and diffusive widths of the interfaces of the grain boundaries, we can resolve the specific grain-boundary diffusivity, D_{GB}, for each type. The diffusive width is used to back out D_{GB} from the simulation quantity $\delta_{GB}D_{GB}$, while the structural width analysis reveals information about possible changes in structural order of the grain boundaries. Calculation of the parameter δ_{GB} shows that a grain boundary with higher energy will exhibit a larger width. We also show that this width remains fairly constant at temperatures from 300 to 450 K. Specifically for the (101) grain boundary, structural and diffusive widths reveal a highly diffusive, disordered structure in comparison to other boundaries in this work. The (201) grain boundary exhibits this to a lesser extent. Parameters necessary to formulate an Arrhenius relation for each grain boundary, such as activation energy and diffusive prefactor, are tabulated.

A directional analysis of the diffusivity in each grain-boundary interface illustrates anisotropy in diffusivity, developing as the h Miller index is increased from 1 to 2 to 4 in (h01). Further analysis of the (401) grain boundary shows that even at low temperatures, it is a fast diffusing interface dominated by structural channels. This is described in two parts. We first show this by examining the slow bulk lattice diffusivity of β-Sn in the crystal's c direction ([001]). In this case, the lattice c direction is perpendicular to the axis of grain tilt ([010]) in the (401) grain boundary, lending very slow diffusion to the boundary in this direction. Second, it is confirmed by inspection of simulation snapshots and knowledge of the boundary's excess energy. For a boundary of such low excess potential energy compared to a bulk structure, and such high diffusivity with low activation energy, stable structural channels must develop in the interface. We see this disorder in only the perpendicular-to-tilt view of the grain boundary. These two observations explain slow diffusion in the perpendicular direction of the interface, and overall low activation energy and fast diffusion in the (401) boundary caused by disordered channels in the parallel direction of the interface.

ACKNOWLEDGMENTS

This research project has been sponsored by the National Science Foundation, under Grants No. CMS-0508854 and No. CHE-0626305, and the United States Navy Office of Naval Research, Advanced Electrical Power Systems. Computing resources were provided by the University at Buffalo Center for Computational Research. We gladly acknowledge the contributions of an anonymous reviewer, whose thorough and conscientious examination of our initial submission of this work led to the discovery and subsequent correction of a significant error in the implementation of the thermostat used to control the temperature of the simulated systems.

[1] P. G. Sutton and P. G. Balluffi, *Interfaces in Crystalline Materials* (Clarendon Press, Oxford, 1995).
[2] P. G. Shewmon, *Diffusion in Solids* (McGraw-Hill Book Company, Inc., New York, 1963).
[3] S. Li and C. Basaran, Comput. Mater. Sci. **47**, 71 (2009).
[4] R. Kirchheim, *Modelling Electromigration and Induced Stresses in Aluminum Lines*, MRS Symposia Proceedings No. 309, (Materials Research Society, Pittsburgh, 1993), pp. 101–110.
[5] S. Li and C. Basaran, Mech. Mater. **41**, 271 (2009).
[6] F. H. Huang and H. B. Huntington, Phys. Rev. B **9**, 1479 (1974).
[7] N. L. Peterson, Solid State Phys. **22**, 409 (1969).
[8] P. H. Sun and M. Ohring, J. Appl. Phys. **47**, 478 (1976), and references therein.
[9] P. Singh and M. Ohring, J. Appl. Phys. **56**, 899 (1984).
[10] C. Basaran, S. Li, D. C. Hopkins, and D. Veychard, J. Appl. Phys. **106**, 013707 (2009).
[11] M. R. Sorensen, Y. Mishin, and A. F. Voter, Phys. Rev. B **62**, 3658 (2000).
[12] A. Suzuki and Y. Mishin, Interface Sci. **11**, 131 (2003).
[13] J. F. Lutsko, D. Wolf, S. Yip, S. R. Phillpot, and T. Nguyen, Phys. Rev. B **38**, 11572 (1988).
[14] A. Suzuki and Y. Mishin, J. Mater. Sci. **40**, 3155 (2005).

[15] G. Ciccotti, M. Guillope, and V. Pontikis, Phys. Rev. B **27**, 5576 (1983).
[16] P. Keblinski, D. Wolf, S. R. Phillpot, and H. Gleiter, Philos. Mag. A **79**, 2735 (1999).
[17] A. U. Telang, T. R. Bieler, J. P. Lucas, K. N. Subramanian, L. P. Lehman, Y. Xing, and E. J. Cotts, J. Electron. Mater. **33**, 1412 (2004).
[18] A. U. Telang, T. R. Bieler, S. Choi, and K. N. Subramanian, J. Mater. Res. **17**, 2294 (2002).
[19] H. Huang, N. Ghoniem, J. Wong, and M. I. Baskes, Modell. Simul. Mater. Sci. Eng. **3**, 615 (1995).
[20] LAMMPS Simulator, http://lammps.sandia.gov (2009).
[21] S. J. Plimpton, J. Comput. Phys. **117**, 1 (1995).
[22] D. Frenkel and B. Smit, *Understanding Molecular Simulation, Second Editon: From Algorithms to Applications* (Academic Press, Elsevier, San Diego, 2002).
[23] J. M. Zhang, X. M. Wei, and H. Xin, Appl. Surf. Sci. **243**, 1 (2005).
[24] Y. Mishin and D. Farkas, Philos. Mag. A **78**, 29 (1998).
[25] M. I. Baskes, Phys. Rev. B **46**, 2727 (1992).
[26] M. I. Baskes, Modell. Simul. Mater. Sci. Eng. **2**, 505 (1994).
[27] R. Ravelo and M. I. Baskes, Phys. Rev. Lett. **79**, 2482 (1997).
[28] NRL Crystal Lattice, http://cst-www.nrl.navy.mil/lattice/ (2009).
[29] J. C. Fisher, J. Appl. Phys. **22**, 74 (1951).